ADVANCED PHYSICS RESEARCH
Open Access
www.advphysicsres.com

Controlling the Crystallization Kinetics of Low Loss Phase Change Material Sb_2S_3

Felix Hoff, Julian Pries, Jan Köttgen, Pierre Lucas, and Matthias Wuttig*

Optoelectronics are crucial for developing energy-efficient chip technology, with phase-change materials (PCMs) emerging as promising candidates for reconfigurable components in photonic integrated circuits, such as nonvolatile phase shifters. Antimony sulfide (Sb_2S_3) stands out due to its low optical loss and considerable phase-shifting properties, along with the non-volatility of both phases. This study demonstrates that the crystallization kinetics of Sb_2S_3 can be switched from growth-driven to nucleation-driven by altering the sample dimension from bulk to film. This tuning of the crystallization process is critical for optical switching applications requiring control over partial crystallization. Calorimetric measurements with heating rates spanning over six orders of magnitude, reveal that, unlike conventional PCMs that crystallize below the glass transition, Sb_2S_3 exhibits a measurable glass transition prior to crystallization from the undercooled liquid (UCL) phase. The investigation of isothermal crystallization kinetics provides insights into nucleation rates and crystal growth velocities while confirming the shift to nucleation-driven behavior at reduced film thicknesses—an essential aspect for effective device engineering. A fundamental difference in chemical bonding mechanisms was identified between Sb_2S_3, which exhibits covalent bonding in both material phases, and other PCMs, such as GeTe and $Ge_2Sb_2Te_5$, which demonstrate pronounced bonding alterations upon crystallization.

1. Introduction

In recent years, technological applications of amorphous/crystalline phase-change materials (PCMs) have undergone a significant transformation, with a notable shift toward their use as reconfigurable components in photonic integrated circuits.[1–5] These materials are distinguished by the high contrast in physical properties between the amorphous and crystalline phases and their rapid and reversible interconversion.[6,7] The high switching speeds and pronounced changes in optical and electrical properties, coupled with the non-volatility of the two states, have previously made PCMs an appealing option for data storage applications.[8–10] While the rapid switching speed is particularly important in these applications, photonic components have somewhat different requirements. For use in photonic integrated circuits, low optical losses (extinction coefficient k close to zero) for both phases at the application wavelength (usually 1550 nm) is a key requirement. Concurrently, the refractive index should exhibit a significant contrast at the operating wavelength upon the phase transition ($\Delta n >> 0$).[11,12] These different requirements for photonic applications have resulted in a notable shift in the type of PCM compounds utilized. While chalcogenides containing tellurium are predominantly employed in electronic data storage applications, chalcogenide compounds containing selenium and sulfur are often preferred for photonic applications.[13–17]

A notable difference in reflectivity exists between the amorphous and crystalline states of Te-containing PCMs. This surprisingly large change exceeds what is expected by the Clausius–Mosotti relation, which describes the impact of the change in density upon the change of optical properties.[18,19] The significant optical contrast observed, can be attributed to a significant change of their chemical bonding upon crystallization.[20,21] In the amorphous phase, these compounds exhibit covalent bonding, while in the crystalline phase, they display metavalent bonding.[20,21] Literature shows that this transition from amorphous covalent to crystalline metavalent bonding plays a crucial role in explaining the pronounced changes in optical properties observed during crystallization.[22,23] Interestingly, significant differences are also observed in the bond rupture as observed by atom probe tomography (APT).[21,24] Metavalent bonded materials are distinguished by a distinctive interplay between the tendency to delocalize electrons, which is characteristic of metallic bonding, and the

---

F. Hoff, J. Pries, J. Köttgen, M. Wuttig
Institute of Physics IA
RWTH Aachen University
52074 Aachen, Germany
E-mail: hoff@physik.rwth-aachen

P. Lucas
Department of Materials Science and Engineering
University of Arizona
Tucson, AZ 85721, USA

The ORCID identification number(s) for the author(s) of this article can be found under https://doi.org/10.1002/apxr.202500005

DOI: 10.1002/apxr.202500005

tendency to localize electrons, which is typical of covalent bonding.[25]

However, the situation is rather different in Se and S-based chalcogenides as these materials exhibit covalent bonding in both the amorphous and crystalline phases.[11] The resulting optical contrast is therefore only determined by the change in density, obeying the Clausius–Mosotti rule, and is consequently moderate, but it is still sufficient to induce phase retardation for applications in optoelectronic signal processing. But most importantly, the large band gaps even in the crystalline state of sulfides and selenides in comparison to Te-based compounds, result in minimal optical losses in the infrared spectrum which enables low loss (extinction coefficient k close to zero), in particular near the operational wavelength 1550 nm.

A large body of literature has recently addressed the optical properties of the amorphous and crystalline phases of Sb_2S_3 and their potential applications in photonic components.[26–29] While the crystallization speed of sulfide compounds is unlikely to reach that of telluride counterparts, the speed of crystallization is still an important parameter for device optimization. In that respect it was recently shown that a correlation exists between the crystallization mechanism of PCMs, i.e., growth versus nucleation control, and the overall speed of crystallization.[30] Nucleation-driven compounds were found to crystallize several orders of magnitude faster. Additionally, a pronounced increase in crystallization stochasticity was observed in pulsed experiments of growth-driven materials.[30] Stochasticity is problematic for applications requiring fine control of the crystallization fraction such as neuromorphic devices.[31] Accessing intermediate states between the binary 0 and 1 open a broad range of advanced applications which may then be prohibited in growth-driven materials. Hence, clarifying the crystallization process in Sb_2S_3 is important for technological applications. Yet, a comprehensive understanding of the transition mechanism in Sb_2S_3 between the amorphous and crystalline phase is still lacking. Furthermore, crystallization speeds reported in the literature vary considerably.[13,14] Hence, we conduct a detailed investigation of this transition in relation to glass dynamics and crystallization kinetics with a focus on determining characteristic parameters for both using differential scanning calorimetry (DSC) and optical microscopy. To that aim, we apply both conventional DSC and ultrafast (flash) DSC (FDSC) to access a sufficiently broad range of heating rates allowing for a clear identification of the relevant thermodynamic features of the phase transition including glass dynamics and crystallization kinetics. The excess heat capacity C_p^{exc} is conventionally obtained by subtracting the heat capacity of the crystal from the heat capacity of the glass.[32] This is based on the approximation that the vibrational heat capacity of the crystal is equivalent to that of the glass. The excess heat capacity C_p^{exc} therefore constitute the configurational component of the heat capacity of the glass. It provides insight on the configurational changes that occurs throughout the glass structure during reheating. Analysis of the glassy and undercooled liquid (UCL) state over a similarly wide range of heating rates uncovers the non-Arrhenius behavior determined by fragility m of the UCL from the determination of the fictive temperature T_f.[33,34] By applying heating rates spanning over six orders of magnitude from 0.03 to 7500 K s^{-1}, the temperature dependence of crystallization is analyzed using Kissinger's method[35,36] from which the activation energy E_K and the temperature-dependent crystallization rate constant k are obtained for bulk glasses. Furthermore, the results from Kissinger's analysis are confirmed using isothermal calorimetric crystallization measurements which yield additional insights on the rate constant k as well as the Avrami exponent n. Isothermally crystallizing thin films of Sb_2S_3 and microscopically observing the crystallization steps of nucleation and growth, also yield the incubation time of nucleation τ, nucleation rate I, crystal growth velocity v_g, final grain density ρ_f, and complete transformation time (CTT). It is found that the phase transformation of glassy powder samples with a bulk thickness of 3 µm is growth-driven, while nucleation plays a more dominant role in the crystallization of thin films with a thickness of 30 nm, especially when the temperature is raised.

2. Results

2.1. Glass Dynamics

The excess specific heat capacity $C_p^{exc}(T)$ measured over a wide range of heating rates for the as-deposited and pre-annealed Sb_2S_3 powder samples is shown in **Figure 1a**. At the lowest heating rate of 100 K s^{-1} in Figure 1a, the excess specific heat capacity $C_p^{exc}(T)$ is initially constant but eventually becomes negative, which is a sign of exothermic heat release due to structural relaxation. $C_p^{exc}(T)$ then shows an endothermic peak (endothermic overshoot) upon transition from the glassy to the UCL state (glass transition). This is followed by a plateau of the UCL and a steep exothermic decent once crystallization commences. All these features increase in temperature as the heating rate is increased, i.e., from 0.03 K s^{-1} (= 2 K min^{-1}) up to 7500 K s^{-1} (= 450 000 K min^{-1}). Measured data from the lowest heating rates are shown in Figure S2 (Supporting Information). The fact that the endothermic overshoot (peak) of the glass transition is observed, demonstrates that Sb_2S_3 crystallizes from the UCL phase similar to $Ge_{15}Te_{85}$ or $Ge_3Sb_6Te_5$[33,37] while contrasting the behavior of conventional Te-based PCMs such as $Ge_2Sb_sTe_5$, GeTe, and AIST.[38–40]

These measurements thus also demonstrate that Sb_2S_3 is in the glassy state at room temperature. Figure 1a furthermore indicates that the endothermic overshoot associated with the glass transition is much more pronounced in the pre-annealed samples. Glasses are known to be prone to aging induced by the mechanism of so-called structural relaxation causing physical properties such as enthalpy, density, or refractive index to evolve with time.[41] The pre-annealing step is therefore expected to induce a significant enthalpy relaxation relative to the as-deposited sample. The recovery of that relaxed enthalpy during reheating then gives rise to the pronounced endothermic overshoot. To investigate that process more systematically, and thus demonstrate how structural relaxation affects the glassy phase of Sb_2S_3, its thermal response is studied as a function of increasing annealing temperature during reheating at 0.67 K s^{-1} (= 40 K min^{-1}) in Figure 1b. Here, measurements of the as-deposited (i.e., unannealed) material are compared to samples that experienced isochronal pre-annealing for 1 h at temperatures T_a ranging from 50 °C to 200 °C. In the as-deposited phase, exothermic heat release upon structural relaxation of the glassy phase during the

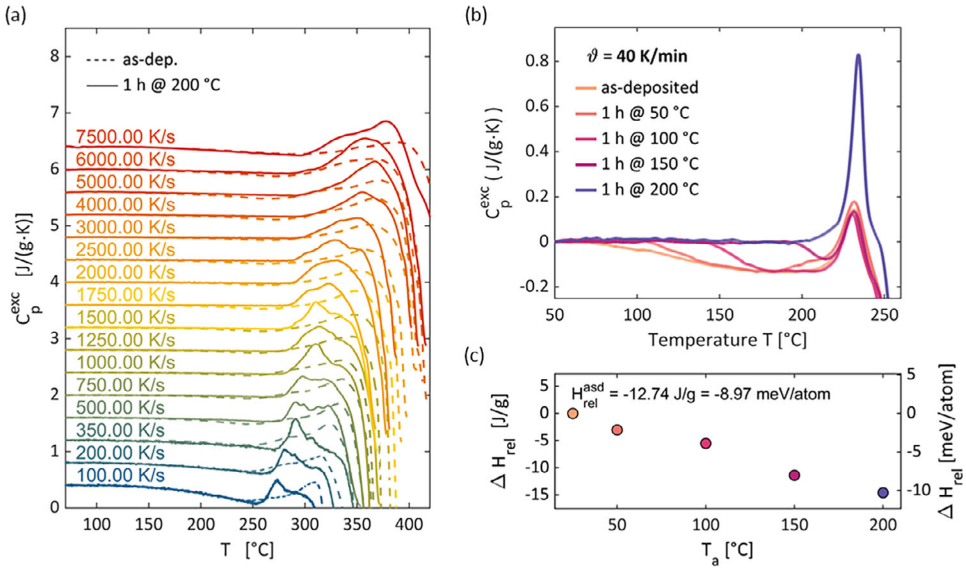

Figure 1. Excess specific heat capacity of Sb_2S_3 for a) heating rates ranging from 100 to 7500 K s^{-1} of the as-deposited and pre-annealed amorphous phase and b) a pre-annealing series measured at 40 K min^{-1}. Increasing the heating rate leads to a change in features of glass dynamics such as a reduction of the exothermic heat release prior to glass transition and an increase in endothermic overshoot. Increasing the pre-annealing temperature in b) while keeping the pre-annealing time fixed at 1 h, structural relaxation occurs whereby enthalpy is released leading to a reduction in the exothermic (negative) regime prior to the glass transition ultimately resulting in an enhancement of the endothermic overshoot upon glass transition. The release of enthalpy in the structural relaxation compared to the as-deposited phase is shown in (c).

upscan is observed to initiate at about 75 °C. This pre-glass transition exotherm is the well-known consequence of the distribution of relaxation times in rapidly quenched glasses.[42] During slow reheating, the fast-relaxing domains of glasses trapped in a high enthalpy state can release enthalpy as they regain mobility and relax toward equilibrium. However, pre-annealing induces relaxation of these domains prior to reheating and should annul that process. Indeed, after pre-annealing at 50 °C, 100 °C, and 150 °C, initiation of enthalpy relaxation is shifted to 100 °C, 140 °C and 190 °C respectively (Figure 1b). After pre-annealing at 200 °C for 1 h, the pre-T_g exotherm is entirely removed and instead a pronounced endothermic overshoot upon the glass transition is observed. This observation indicates that pre-annealing at increasing temperature T_a induces relaxation of increasingly slow domains thereby lowering the fictive temperature T_f as well as the enthalpy state until eventually, no exothermic relaxation can occur at the specified heating rate and all the relaxed enthalpy is instead regained at the glass transition (endothermic overshoot).[41,43] The enthalpy release can be quantified from the integral of the difference between the pre-annealed and the as-deposited excess specific heat capacity and is indeed found to increase with increasing T_a as illustrated in Figure 1c. At pre-annealing temperatures higher than 200 °C, the crystallization process is already initiated during pre-annealing, as shown in Figure S1 (Supporting Information).

The behavior observed in Figure 1a–c shows that the glassy phase is strongly influenced by the thermal history. Structural relaxation leads to several different glassy states which vary over a broad range of physical properties such as viscosity, electrical conductivity, density, and others.[41,44–46]

2.2. Cooling Rate Dependent Fictive Temperature and Calorimetric Fragility

The data of Figure 1a–c also establish that Sb_2S_3 undergoes a clear calorimetric glass transition and that the UCL state can be accessed. This permits to study the glass dynamics in more detail to determine the (standard) glass transition temperature $T_g^{(s)}$ and thermodynamic fragility m. These parameters are in turn sufficient to describe the temperature dependence of the viscosity $\eta(T)$ of the UCL, which is useful to simulate and possibly optimize crystallization. **Figure 2a** shows that there is a plateau in the temperature range between the glass transition and the onset of crystallization. Entering this plateau means that the material is in now its UCL phase where the thermal history of the glassy state is erased. Since the UCL of Sb_2S_3 can be accessed, well-defined glassy states can be generated by cooling from the UCL state at various constant cooling rates ϑ. If the same rate is then used to reheat the newly created glass state, the resulting glass transition temperature is then equal to the fictive temperature of the glass formed at this (cooling) rate $T_f(\vartheta)$.[34,47] This permits to measure the (cooling) rate dependence of the fictive temperature $T_f(\vartheta)$ which in turn yields the thermodynamic fragility of (undercooled) liquid Sb_2S_3 as shown below. This also provides the (standard) glass transition temperature T_g^s defined as the fictive temperature $T_f(\vartheta)$ at 20 K min^{-1}.

The data obtained from these $\vartheta_c = \vartheta_h$ measurements are presented in Figure 2b. As illustrated, the shift of the glass transition to higher temperatures for higher heating rates is also evident in this instance. This behavior is linked to the kinetic nature of the glass transition.[48] By employing an onset determination

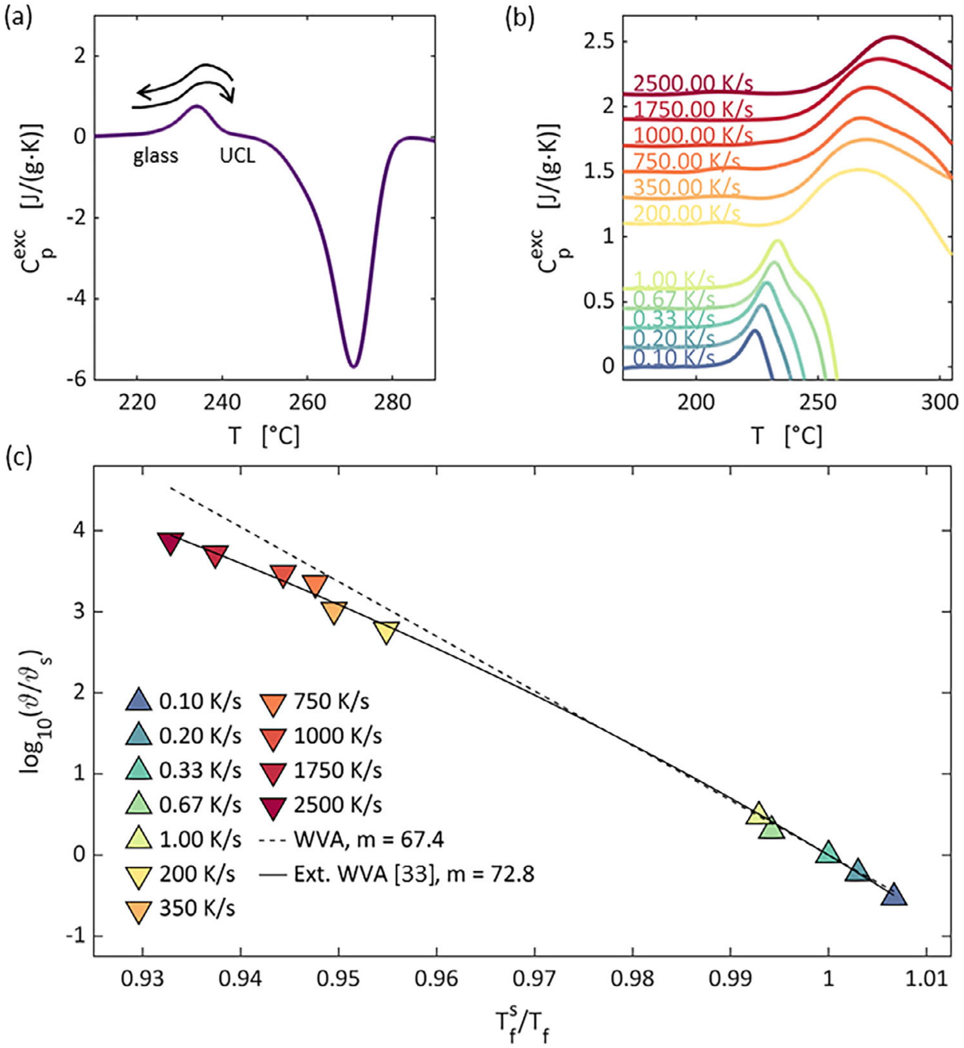

Figure 2. a) Excess specific heat capacity of Sb_2S_3 at heating rate of 40 K min^{-1}. Three distinct temperature ranges can be identified, within which the three different material phases (glass, UCL, and crystal) are present. The arrows indicate the process for generating defined glass states. b) Upscan glass transition peaks at which the heating rate corresponds to the rate at which the glass state was generated. c) Dependence of the fictive temperature as a function of the heating rate, scaled to the standard fictive temperature and the standard heating rate of 20 K min^{-1} respectively. Fit using the Wang, Velikov, and Angell (WVA) equation shown as a dashed line, fit using the extension with the Vogel–Fulcher–Tammann (VFT) model[33] shown as a solid line, provides values for the thermodynamic fragility *m*.

methodology to measure the glass transition temperature, it is possible to determine the fictive temperatures T_f as a function of the cooling rate ϑ_c. Given that the heating rate at which the data was recorded is equal in magnitude to the cooling rate at which the glassy states are generated ($\vartheta_h = \vartheta_c$), it can be concluded that the fictive temperatures are equal to the glass transition temperatures ($T_f = T_g$) that are determined from the data.[49] The glass transition (fictive) temperature at the standard heating rate ϑ_s of 20 K min^{-1} (0.33 K s^{-1}) is designated as the standard glass transition temperature $T_g{}^s$ and was determined thereby to be 217.4 °C.

For heating rates close to this standard heating rate, a model proposed by WVA can be employed to find the thermodynamic fragility *m*, which describes how rapidly the dynamics of the system accelerate when it is heated above its glass transition temperature as described by the WVA equation.[50]

$$\log_{10}\left(\frac{\vartheta}{\vartheta_s}\right) = m\cdot\left(1-\frac{T_f}{T_f^s}\right) \tag{1}$$

where $T_g{}^s = T_f{}^s$. Figure 2c shows the fictive temperatures determined as a function of the heating rate using the WVA. The data points close to the standard heating rate ϑ_s are shown as triangles pointing upwards. A linear regression using the WVA equation can be used to determine the fragility, resulting in a value of *m* = 68 and the corresponding dashed line in Figure 2c. While the dashed line describes the data close to ϑ_s well (upward-pointing triangles), the data measured at high rates (downward-pointing triangles) are not described adequately. To address these apparent limitations of the WVA equation's heating rate range, an extension incorporating the non-Arrhenius behavior of the UCL as derived in literature[33] is adopted here which states

$$\log_{10}\left(\frac{\vartheta}{\vartheta_s}\right) = \log_{10}\left(\frac{\eta_s}{\eta\left(T_f\right)}\right) \tag{2}$$

where η_s is the viscosity at the standard glass transition temperature and $\eta(T_f)$ is the viscosity of the UCL at the fictive temperature T_f of the glass formed during cooling at ϑ.[33] Now a function describing the temperature dependence of the viscosity of the UCL like the VFT model for $T = T_f$ can be inserted into Equation (2). Its parameters can then be optimized to fit the experimental data. Using the VFT equation of $\eta(T) = \eta_\infty \exp(-\frac{D \cdot T_0}{T - T_0})$,[51–53] where η_∞ is the (extrapolated) viscosity of the UCL in the infinite temperature limit and D and T_0 are fitting parameters, Equation (2) can be fitted to the data. Since D and T_0 are linked to the standard fictive temperature T_f^s (= standard glass transition temperature) and the fragility m,[47,54] its values can be calculated from the fitting results. Thus the extension proposed in literature[33] enables the inclusion of data points at elevated cooling and heating rates differing largely from ϑ_s as is the case for FDSC (downward-pointing triangles in Figure 2c) by adopting the non-Arrhenius behavior of the UCL. Fitting the equation from literature[33] to the data obtained around and far away from ϑ_s yields the solid line in Figure 2c, which describes all the data quite well and results in a value for the fragility of $m = 73$.

Other studies have reported similar values for the glass transition temperature (T_g = 219 °C[55] and T_g = 232 °C[56]) and a fragility of $m = 59$.[55] This value is consistent with the classification of the material in a region between those that are ideally strong (low m), such as SiO_2 with $m = 20$,[57,58] and those that are fragile (high m), such as antimony and tellurium-based PCMs (e.g., $Ge_2Sb_2Te_5$, $m = 98$[38]). The reduced glass transition temperature $T_{rg} = T_g/T_m$ for Sb_2S_3 is approximately 0.60 (using melting temperature from literature[56]), which is at the upper end of the values typically found for tellurium-based, metavalently bonded PCMs, ranging from 0.48 to 0.61.[18,59] This indicates that Sb_2S_3 is an effective glass-former, suggesting it possesses high thermal stability and low volatility, but also exhibits a slower crystallization rate.

The heating rate dependence of the fictive temperature across a broad range of heating rates has been established in this study. These insights are crucial for photonic applications, which involve high heating and cooling rates. Consequently, the ability to predict vitrification and thus switching from crystalline to amorphous (glassy phase) via the UCL is essential.

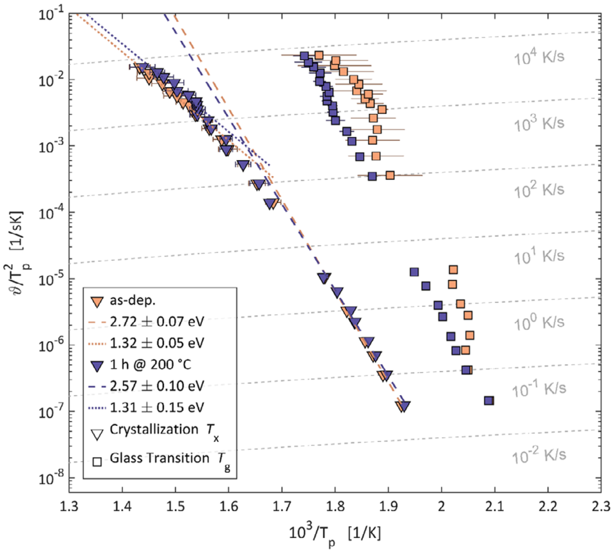

Figure 3. Kissinger plot showing the peak temperature of crystallization T_x (triangles) for both as-deposited and pre-annealed Sb_2S_3 obtained at constant heating rates. The curvature of the data indicates that there is no strict Arrhenius behavior exhibited over the entire heating rate range under consideration. In order to determine the activation energy, it was assumed that Arrhenius behavior would be exhibited over two distinct heating rate ranges. As can be observed, the activation energy decreases as the heating rate increases. It is notable that the activation energies of the as-deposited and pre-annealed phases are in alignment within their respective error margins. Furthermore, it is evident that the glass transition onset temperatures T_g are considerably lower than the peak temperature of crystallization across all applied heating rates.

2.3. Calorimetric Crystallization at Constant Heating Rate

PCMs are usually observed to crystallize from the glassy phase where crystallization initiates prior to the glass transition.[38–40] As a consequence, an alteration in glassy state, e.g., by structural relaxation during pre-annealing, will lead to a reduction in crystallization speed.[38–40,60–63] Given that the crystallization speed of Sb_2S_3 is reported to be less than that of other PCMs,[13] a further reduction in crystallization speed caused by structural relaxation of the glassy phase would be detrimental to the viability of Sb_2S_3 for data storage and photonic applications. Conversely, if crystallization in Sb_2S_3 occurs from the UCL phase, where the thermal history of the glassy phase has been erased upon entering the UCL, it can be reasonably assumed that crystallization should not be affected by pre-annealing (assuming that a change in subcritical grain distribution does not significantly impact crystal nucleation behavior and hence remains small). To test for any changes in crystallization speed induced by structural relaxation of the glassy phase, the measurements presented in Figure 1a were repeated for at least another nine times at each heating rate applied and the crystallization peak temperature T_x was measured. Additional data of the excess specific heat capacity in the low heating range regime are shown in Figure S2 (Supporting Information). A Kissinger's analysis of these measurements yields the heating rate ϑ dependence of the crystallization temperature T_x from which the temperature dependence of crystallization can be inferred using Kissinger's equation:

$$\ln\left(\frac{\vartheta}{T_x^2}\right) = -\frac{E_K}{k_B T_x} + \ln\left(k_0 \frac{k_B}{E_K}\right) \tag{3}$$

where E_K is the Kissinger activation energy of crystallization, k_B the Boltzmann constant and k_0 the prefactor of the rate constant $k(T)$.[35,36,64–66]

The heating rate dependence of the crystallization peak temperature T_x of as-deposited and pre-annealed Sb_2S_3 is depicted in **Figure 3** (orange and purple triangles, respectively). For all applied heating rates, the values for T_x are almost identical for both glassy phases. This observation is in line with the finding from above of crystallization occurring from the UCL subsequent to the transition from a glassy state to undercooled melt where the glassy state and its thermal history is erased. This observation is incompatible with crystallization from the glassy phase prior to glass transition, where structural relaxation upon pre-annealing would have caused the viscosity to increase, largely hampering atomic diffusivity and thus slowing down crystallization. In such case, a shift in T_x to higher temperatures compared to the unannealed (as-deposited) case at the same constant heating rate would be expected but is not observed.

Additionally, the values of T_x with and without pre-annealing show a curved behavior where the slope is reduced at higher heating rates. By fitting the Kissinger equation (Equation 3) to the crystallization temperature data, the activation energy of the crystallization process can be determined for the low and high end of heating rates applied, see Figure 3. The activation energy of crystallization at low ϑ in the range of 0.03 to 3.33 K s^{-1} was found to be 2.72 eV $\pm$ 0.07 eV for the as-deposited phase and 2.57 eV $\pm$ 0.10 eV for the pre-annealed phase, as is illustrated by the dashed lines. For the high heating rates (1000 to 7500 K s^{-1}), the activation energy was found to be 1.32 $\pm$ 0.05 eV for the as-deposited phase material and 1.31 $\pm$ 0.15 eV for the pre-annealed material. For both heating rate regimes, the activation energies are found to be similar or almost identical within the limits of experimental error for the two distinct amorphous glass phases. At the higher heating rates, the agreement is even more evident. The equality of the Kissinger activation energy combined with the similarity in T_x values of as-deposited and pre-annealed Sb_2S_3 in both heating rate regimes demonstrates that the temperature dependence of crystallization is identical for both material phases at all heating rates. As stated above, this behavior is to be anticipated for materials that do not crystallize from the glass phase directly, but rather from the UCL phase. Given that the UCL exhibits quasi-ergodic behavior,[67] the temperature dependence must be identical for both, as-deposited and pre-annealed measurements. Consequently, the distinct glassy states have no impact on the crystallization process Sb_2S_3 unlike in conventional PCMs such as $Ge_2Sb_2Te_5$, AIST, and GeTe.[38,40,68] Any observed differences may only arise from alterations in the initial sub-critical nuclei distribution induced by thermal treatment and difference in initial nucleation rate I that it causes. However, as can be seen from Figure 3, this effect seems to be rather low in Sb_2S_3, if present at all.

From the excess specific heat capacity C_p^{exc} measurements at the various heating rates applied, the glass transition temperature can be measured from the apparent onset of the glass transition. The results are also presented in Figure 3 for as-deposited and pre-annealed Sb_2S_3 (orange and purple squares, respectively). Like the behavior of the glass prior to the glass transition seen in the C_p^{exc} curves, the apparent onset of the glass transition is also heavily affected by thermal treatment and thus the structural relaxation the glassy state experienced. Glassy states are especially susceptible to sub-glass transition pre-annealing when the fictive temperature T_f of the glassy phase is high, which implies a low relaxation time τ allowing for fast structural relaxation. The amorphous phases investigated here were not produced by rapid cooling from a liquid phase; rather, they were created through magnetron sputter deposition. Additional research on chalcogenide glasses and their properties prepared by magnetron sputter deposition also demonstrated elevated fictive temperatures of the as-deposited amorphous state which indicate small relaxation times τ of the as-deposited phase, accompanied by a considerable release of enthalpy through structural relaxation preceding the glass transition.[33,37,39] If the as-deposited amorphous phase shows much smaller relaxation times, the apparent onset of the glass transition should be observed earlier upon heating at a constant rate compared to pre-annealed glasses where the relaxation time is larger and changes induced to the glass during the upscan appear later causing the apparent onset of glass transition to shift to higher temperature explaining the observation shown in Figure 3. In summary, the pre-annealing process, which results in a significant structural relaxation of the glassy phase (see Figure 1c), exerts a pronounced influence on the apparent onset of the glass transition but not on the crystallization peak temperature T_x in Sb_2S_3 as crystallization occurs from the UCL.

2.4. Calorimetric Crystallization at Isothermal Conditions

To gain further insight into the crystallization process, crystallization kinetics were studied at isothermal conditions at five different heating temperatures while the heat flux was measured calorimetrically. Thereby the rate of enthalpy release was measured by DSC and then integrated over time. As stated by Borchardt and Daniels, the enthalpy released during crystallization is directly proportional to the crystallized volume fraction $\chi(t)$.[69] Accordingly, the crystallized volume fraction $\chi(t)$ as measured from the released enthalpy is shown in **Figure 4**a. As expected, the material crystallizes faster the higher the temperature. Assuming the crystal growth rate at isothermal conditions is constant and shows no transient behavior, a simple expression can be used to describe the crystalline volume fraction[70–74]

$$\chi(t) = 1 - \exp\left(-(k \cdot t)^n\right) \tag{4}$$

The exponent n is the Avrami exponent. The crystallized volume fraction data in conjunction with this equation can be used to construct an Avrami plot as shown in Figure 4b. Linear regression, which is able to describe the data reasonably well, allows to determine the Avrami exponent n and the rate constant k.[71–73] The results for the rate constant of these fits are shown in Figure 4c. An Avrami exponent n being very close to 3 (as can be seen in Figure S3, Supporting Information) indicates constant (time independent) crystallization behavior driven by crystal growth rather than transient nucleation.[75,76] Additional analysis of how temperature affects incubation time can be found in Supporting Information.

The activation energy resulting from the rate constant of isothermal crystallization in the considered temperature range is 2.64 $\pm$ 0.13 eV. This value is in good agreement with the Kissinger activation energy of 2.52 to 2.72 eV in the low heating rate regime (Figure 2). This shows consistent crystallization behavior for crystallization under constant heating rate in the low heating rate regime and isothermal crystallization at the selected (low) temperatures. Interestingly, the activation energy agrees with the results of isothermal crystallization on about 150 nm thick films

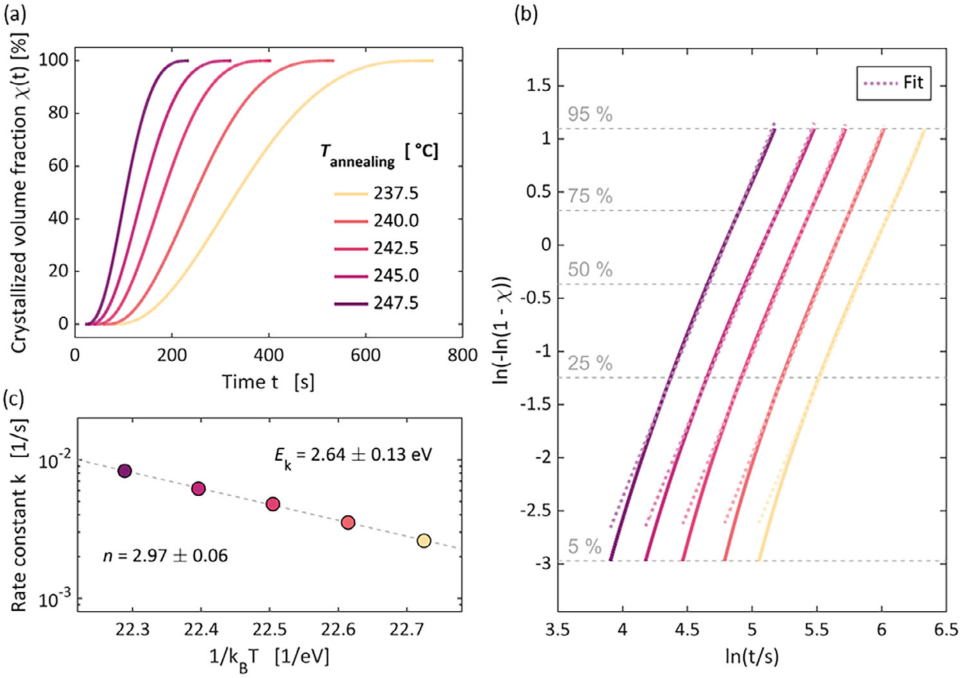

Figure 4. a) Isothermal crystallization at five temperatures. As expected, the material crystallizes more rapidly at higher temperatures. b) Avrami plot of crystallized volume fraction $\chi(t)$. Linear regression in the Avrami plot leads to the Avrami exponent n and the rate constant k, as shown in the Arrhenius plot in (c).

from the literature.[77] An activation energy of 2.64 eV is found there, as well as a low Avrami exponent of less than 3. The crystallization temperatures in this study are 20 °C higher, which is to be expected with the reduction in film thickness.[77]

2.5. Isothermal Crystallization of Thin Films

From the Avrami exponent determined in the previous section, the dimensionality of the crystallization process as well as the interplay of the activation energy of nucleation and crystal growth velocity can be inferred: $n = 3$ in a three-dimensional crystallization process means that crystallization occurs from a fixed number of nucleation sites from which grains grow (expand in size) and that the activation energy determined above describes the activation energy of the crystal growth velocity E_v. Therefore, these results suggest that the vast majority of grains should nucleate at the beginning of the crystallization process and that the temperature dependence of the crystal growth velocity in Sb_2S_3 should be determined by $E_k = E_K = E_v$. To substantiate this hypothesis, crystallization is investigated microscopically where it is possible to measure nucleation rate I and crystal growth velocity v_g directly at various isothermal heating temperatures and observe the temperature dependence of v_g this way. This approach will moreover allow for the determination of the incubation time τ of crystal nucleation, the final grain density ρ_f, the complete crystallization time (CTT) and the rate constant k as well as their temperature dependence and will thus yield a more detailed and integrated picture.

Specimen for the investigation of crystallization kinetics in Sb_2S_3 by optical microscopy were prepared by thin film deposition with an approximate thickness of 30 nm on a Si_3N_4-coated Si substrate. Additionally, a sandwich layer of $(ZnS)_{80}$:$(SiO_2)_{20}$ is applied to the Sb_2S_3 to prevent oxidation. Having the Sb_2S_3 sandwiched in between the same material ensures that the surface energy of the Sb_2S_3 is the same for both interfaces. If the surface energy of both interfaces is identical so should be the nucleation behavior of both interfaces. The layer thicknesses of all layers involved were selected to maximize the optical contrast between the amorphous and crystalline phases in the visible spectrum. A sketch of the layer stack is shown in Figure S5 (Supporting Information).

Each sample was heated isothermally at a set heating temperature for a certain time interval after which it was investigated and photographed under an optical microscope and subsequently heated and investigated again, and so on. In total four samples were investigated at the heating temperatures of 220 °C, 225 °C, 230 °C, and 235 °C, respectively. The temperatures were set below the temperatures which were used for the measurements shown in Figure 4 (isothermal calorimetry) to allow sufficient time for the crystallization process to occur, and to enable observation of the transformation process on laboratory time scales. **Figure 5** illustrates the effect of gradual heating at the lowest of these temperatures, namely 220 °C. As can be observed in the figure, the transition from the amorphous as-deposited phase to a large crystallized volume or area fraction state is evident as the heating time is increased from left to right. It is evident that the distinction between the amorphous and crystalline phases is easily possible, allowing for a detailed examination of the nucleating and growing crystallites. Additionally, light microscope images corresponding to the other three temperatures are presented in Figure S6 (Supporting Information).

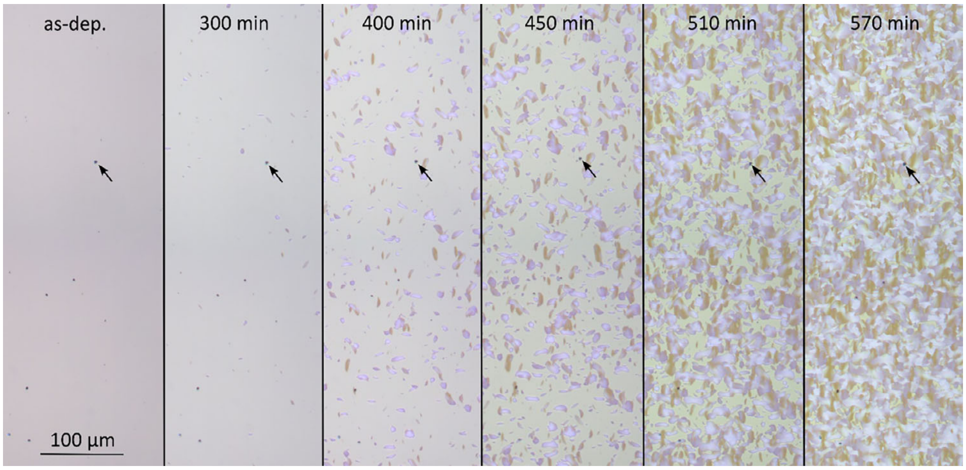

Figure 5. Light microscope images of the Sb_2S_3 thin film sample, heated at 220 °C. Shown is the evolution from induction of first grains to almost complete crystallization. The amorphous material has a gray color. The crystallites appear in two colors, pink and brown, which are associated with the anisotropic dielectric properties of the material. Arrows have been added to each image to highlight a dirt particle, indicating consistent location across all heating steps.

The incubation time of crystal nucleation τ can be understood as the time period at the heating temperature applied, that needs to pass until the first (microscopically measurable) grain forms while the CTT is the time interval from 1 % to 99 % of crystallized volume fraction and can be measured from the Avrami plot as shown in Figure S7 (Supporting Information). In other words, the CTT is the duration of the crystallization process. Both, τ and CTT can be easily determined via the time course of the number of grains formed and amorphous area fraction, respectively (see Figure S7, Supporting Information). The results for τ, CTT, I, ρ_f, ν_g, and k are shown as a function of inverse temperature in **Figure 6a–f**, respectively. As expected, it can be observed that crystallization starts earlier and progresses more rapidly when T is raised as the increase in I and ν_g as well as the decrease in τ and CTT show. This behavior is in line with what has already been observed in the case of the isothermal calorimetric measurements on samples several micrometers thick.

Additionally, the nucleation behavior is investigated simply by counting the number of newly formed crystal grains in the remaining amorphous regions at each heating step and dividing the change in number of grains by the time of the heating interval and the remaining amorphous area. The final grain density ρ_f is found from the sum of all nucleated grains within the investigated area at the stage of complete crystallization.

In Figure 6d a clear increase in final grain density ρ_f is evident as temperature is increased, which demonstrates that the

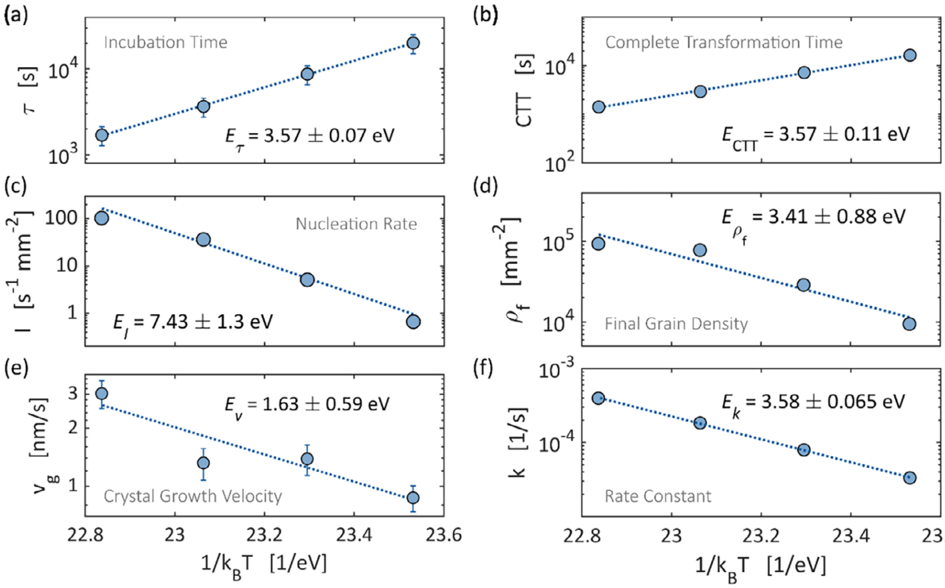

Figure 6. a) Incubation time τ, b) complete transformation time (CTT), c) nucleation rate I, d) final grain density ρ_f, e) crystal growth velocity ν_g, and f) rate constant k determined for the four different temperatures 220 °C, 225 °C, 230 °C, and 235 °C.

nucleation process becomes more pronounced as compared to the growth process when temperature is increased. This is also reflected by the increase of two orders of magnitude in the average nucleation rate I when the temperature is raised from 220 °C to 235 °C, as shown in Figure 6c, whereas v_g only increases by a factor of 3. While the values for the nucleation rate I presented here constitute the average of all measured values at the heating temperature, for the transient behavior please refer to Figure S7 (Supporting Information), where the nucleation rate plotted as a function of time initially rises sharply, reaches a maximum, and then decreases slightly when crystallization completes.

From the crystallized area fraction data shown in Figure S7 (Supporting Information) we can furthermore deduce the rate constant k, see Figure 6f, from which we can find the activation energy of the rate constant E_k and the Avrami exponent n for the 30 nm thick specimen investigated here. The values for E_k and n are determined to be 3.58 ± 0.07 eV and about 10, respectively (see Figure S7f, Supporting Information). These values differ significantly from the values obtained from the calorimetric measurements at low constant heating rate and under isothermal conditions where E_k was about 2.6 eV and $n =$ 3. While in the case of the thick samples investigated in calorimetric measurements, crystal growth governs crystallization, for thin films of Sb_2S_3 the Avrami exponent of around 10 suggests, that the nucleation rate is dominating the crystallization process. It could even be accelerating with time and thus shows a transient increase during the crystallization process,[76] as observed here (see Figure S7, Supporting Information). The difference in E_k yields additional evidence that the crystallization process has changed drastically upon going from 3 μm thick samples to 30 nm thin films.

Furthermore, the crystal growth velocity v_g is illustrated in Figure 6e as a function of temperature. Going from 220 °C to 235 °C, the growth velocity only increases slightly from approximately 1 to 3 nm s^{-1}. The crystal growth velocity is related to the average grain size evolution shown in Figure S7a (Supporting Information). The small increase in crystal growth velocity v_g (factor of 3) compared to the large increase in nucleation rate I (almost three orders of magnitude) supports the hypothesis of crystallization being governed by the accelerating nucleation behavior. This conclusion is also supported by the high Avrami exponent of about 10, which constitutes additional evidence that the crystallization behavior in thick flakes (calorimetric investigation) and thin films (microscopic investigation) differ significantly.

The comparison of the two series of measurements on thick powder samples with a thickness of 3 μm and confined thin-film samples with a thickness of 30 nm reveals notable discrepancies in the crystallization behavior observed. While crystal growth is the primary driving force behind the phase transformation of the powder samples, nucleation plays a dominant role in the crystallization of the thin films. A change in the surface-to-volume ratio as well as in surface energy occurs when transitioning from thick flakes to thin film samples. As is evident from the data, an increase in this ratio and the change in surface energy has a pronounced effect on the nucleation process. The literature discusses scenarios where a capping layer is deposited on top of Sb_2S_3 films with a Si substrate at the bottom. In this case, the capping layer has been shown to inhibit crystal growth while promoting nucleation.[78] In the present study, the film thickness is reduced and a capping layer is introduced to the top and bottom of the material. Therefore, we cannot distinguish the effect of each on nucleation from our measurements alone. It is reasonable to assume that heterogeneous crystallization at the interfaces influences the crystallization mechanism toward increased nucleation activity. Therefore, it is crucial to consider the implications of this observation on potential applications in nanoscale photonic devices, as design changes can have a large impact on device performance due to the modified crystallization behavior.

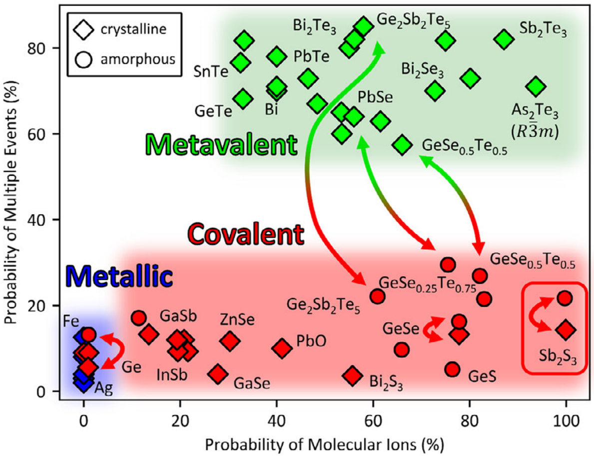

Figure 7. PME and PMI for amorphous (circles) and crystalline (diamonds) solids, measured by atom probe tomography (APT). Metals evaporate without any molecular ions. In contrast, covalent systems can show a large amount molecular ions. In particular in this point Sb_2S_3 stands out, as it evaporates almost solely in molecular fragments. For metavalently bonded crystalline chalcogenides, the PME changes significantly upon vitrification (arrows); this is not the case for other solids. The figure and data were adapted[21] and extended with the data measured here for amorphous Sb_2S_3.

2.6. Understanding the Crystallization of Sb_2S_3 from a Bonding Perspective

Building on these insights into the crystallization behavior of thick flake powders and confined thin film samples, it is beneficial to delve deeper into the unique bonding characteristics that influence the crystallization processes in different materials, with a particular focus on the differences between Sb_2S_3 and telluride-based PCMs. Crystallization in Sb_2S_3 clearly differs from crystallization in Te based phase change materials like GeTe, $Ge_2Sb_2Te_5$ and Sb_2Te_3. These tellurides are characterized by a pronounced change of their bond rupture in APT upon crystallization. This finding is illustrated in **Figure 7**, which presents two distinct characteristics for a series of amorphous and crystalline solids. The first characteristic is the probability that a fragment is a molecule and not a single atom (PMI). The second characteristic is the probability that the number of fragments formed upon a successful laser pulse is larger than one,[21,24] i.e., the probability of multiple events (PME). The working principal of the APT as well as PMI and PME are explained in more detailed in Figure S8 (Supporting Information). Note that the data points in Figure 7 other than the amorphous Sb_2S_3 have already been published in one of our previous works.[21] The PME is high for crystalline phase change materials such as GeTe or $Ge_2Sb_2Te_5$. This has been shown to be related to a bonding mechanism which leads to unconventional properties such as a pronounced optical absorption, a large Grüneisen parameter for transverse optical modes, a measure of bond anharmonicity, and a high Born effective charge, indicative for a pronounced chemical bond polarizability.[21,24,79] Amorphous GeTe and $Ge_2Sb_2Te_5$ on the contrary do not possess these unconventional properties and instead reveal the more ordinary property portfolio of covalently bonded solids.[80]

This is in line with observations in atom probe tomography. APT shows a much smaller PMEs for these amorphous solids (Figure 7). Hence, for phase change materials such as $Ge_2Sb_2Te_5$, $GeSe_{.25}Te_{.75}$, or $GeSe_{.5}Te_{.5}$, a significant change of bonding accompanies crystallization.[81] This is highly unusual, since it has been argued already almost a century ago that iono-covalent solids such as SiO_2 do not change their bonding upon crystallization.[82] The corresponding glasses are frequently denoted as Zachariasen glasses. Most phase change materials such as GeTe or $Ge_2Sb_2Te_5$ do not fall into this category. Their glasses differ from the corresponding crystalline phases, i.e., form non-Zachariasen glasses. We have thus also studied amorphous and crystalline Sb_2S_3 with the atom probe tomography. Sb_2S_3 reveals a different behavior than, e.g., GeTe. Both the amorphous and crystalline phase show a low PME, characteristic for covalent bonds. This implies that for Sb_2S_3 no change of bonding upon crystallization occurs, in line with the rather moderate change of properties upon crystallization. Figure 7 summarizes these findings for a significant number of solids. Circles depict amorphous (glassy) solids, while diamonds present crystalline phases. This figure clearly shows that crystalline PCMs such as GeTe, Sb_2Te_3, and $Ge_2Sb_2Te_5$ and a number of other chalcogenides, often based on tellurides, such as PbTe, Bi_2Te_3, and $AgSbTe_2$ are characterized by a large PME. Metals, and covalently bonded semiconductors, instead show a significantly smaller PME, as do crystalline chalcogenides such as GeSe, GeS, Bi_2S_3, and Sb_2S_3. Interestingly, all amorphous (glassy) solids also possess a small PME, including Sb_2S_3 and GeSe. Hence, for a few chalcogenides such as $Ge_2Sb_2Te_5$, there is a pronounced change of bonding upon crystallization (as seen by APT), which is neither the case for GeSe and Sb_2S_3. It has been observed that the tellurium-based PCMs, which demonstrate a transition from covalent to metavalent bonds, exhibit rapid crystallization.[18,59] In contrast, the sulfur and selenium-based PCMs, which exhibit a transition from covalent to covalent bonds, demonstrate slower crystallization.[13,18] This observation aligns with the properties of Sb_2S_3 discussed in this study.

3. Conclusion

A combined investigation of the glass dynamics and crystallization kinetics of Sb_2S_3 reveals that the material exclusively crystallizes from the UCL phase. This indicates that the crystallization process is independent of the thermal history of the glassy phase and how much aging and structural relaxation it has experienced. This is beneficial for non-volatile components in photonic integrated circuits since it increases the repeatability upon switching and after long term storage at elevated temperatures. Unlike phase change materials such as GeTe, Sb_2Te_3, and $Ge_2Sb_2Te_5$, crystallization is not accompanied by a change of bonding in Sb_2S_3, as confirmed by atom probe tomography. Additionally, it was determined that the crystallization process differs in thin films and micrometer thick material. In contrast to the latter material, which undergoes a growth-driven crystallization process, the thin film exhibits a nucleation-driven transformation. This is a beneficial property for device engineering, as it prevents stochasticity of the crystallization process and should therefore enable a fine control of the fraction of crystallization for multistate applications. Moreover, the prevention of large crystal grains mitigates the detrimental topography effects that may arise in optoelectronic applications from the anisotropic crystal structure.

Upon increasing the temperature, Sb_2S_3 always enters the UCL prior to crystallization, allowing the fictive temperature to be determined over a wide range of heating rates. This enables determination of the standard glass transition temperature, the heating rate dependence of the fictive temperature, and the thermodynamic fragility m of the system. These parameters agree with literature values and are central for modeling the temperature dependence of the viscosity of the UCL phase of Sb_2S_3. Given the close relationship between viscosity, nucleation rate, and crystal growth rate, this modeling is crucial for simulating photonic devices and their switchability from low to high temperatures.

4. Experimental Section

Powders for conventional DSC and FDSC measurements of the phase change material (PCM) Sb_2S_3 are produced from a stoichiometric target by magnetron sputter deposition at a base pressure of 3×10^{-6} mbar. The powder samples were sputtered as a 3 µm thick film. This as-deposited material was subsequently peeled off the substrate and ground into small particles by stirring the flakes with a spatula in a glass vial. The thickness of these powder flakes is determined using in-plane scanning electron microscopy (SEM) measurements, as illustrated in Figure S9 (Supporting Information). The thin-film samples were produced under comparable conditions, but with a significantly shorter deposition time. The correct stoichiometry and composition of the samples were confirmed by atom probe tomography and XRD analysis, as shown in Figures S10–S12 (Supporting Information). The excess specific heat capacity C_p^{exc} was obtained in a PerkinElmer Diamond DSC and a Mettler-Toledo Flash DSC 1 by subtracting the crystalline rescan from the initial scan. The as-deposited and pre-annealed Sb_2S_3 samples were measured on two sensors in FDSC. The melting onset of pure Indium was used to calibrate the temperature at a constant heating rate ϑ of the DSC and FDSC measurements. DSC, FDSC, and XRD data showed no evidence of phase separation during crystallization. The investigation of crystallization kinetics by optical microscopy involved adding thermal energy in time steps, with images captured after each step to monitor grain formation and growth. Nine overlapping images were taken per heating step, covering an area slightly larger than 1 mm^2. Grain diameters and numbers were determined manually using an open source graphics program (GIMP), where grains were counted and marked to track changes between heating steps. Needle-shaped specimens were prepared by SEM-FIB dual beam focused ion beam (Helios 650, FEI) using the standard "lift-out" method with an in situ Pt capping via the GIS. APT measurements were conducted on a LEAP 5000XS (CAMECA) by applying a UV laser (wavelength = 355 nm) pulse with a laser pulse energy of 5 pJ, a pulse repetition rate of 125 kHz, a specimen base temperature of 40 K and an average detection rate of 1.0%. APT data reconstruction was processed with the commercial software APSuite 6.3.1. Multiplicity analysis was conducted using the in-house MATLAB package EPOSA.

Supporting Information

Supporting Information is available from the Wiley Online Library or from the author.

Acknowledgements

F.H. and M.W. acknowledged financial support from NeuroSys as part of the initiative "Clusters4Future", which was funded by the Federal Ministry of Education and Research BMBF (03ZU2106BA). P.L. acknowledged financial support from the National Science Foundation NewFoS STC award # 2242925.

Open access funding enabled and organized by Projekt DEAL.

Conflict of Interest

The authors declare no conflict of interest.

Author Contributions

F.H. performed sample preparation, XRD, DSC, FDSC, and light microscope investigation and data curation, formal analysis, wrote the original draft, reviewed and edited the writing. J.P. worked on conceptualization, project administration, sample preparation, formal analysis, significantly reviewing and editing, developing data analysis scripts using Matlab. J.K. worked on atom probe tomography and SEM measurements and data analysis. M.W. and P.L. provided supervision, reviewed, and edited the writing-. All authors have given approval to the final version of the manuscript.

Data Availability Statement

The data that support the findings of this study are available from the corresponding author upon reasonable request.

Keywords

crystallization kinetics, fragility, glass dynamics, glass transition, metavalent bonding, phase change materials

Received: January 19, 2025
Revised: February 28, 2025
Published online:

---

[1] R. Chen, Z. Fang, C. Perez, F. Miller, K. Kumari, A. Saxena, J. Zheng, S. J. Geiger, K. E. Goodson, A. Majumdar, *Nat. Commun.* **2023**, *14*, 3465.
[2] Z. Fang, R. Chen, J. Zheng, A. Majumdar, *IEEE J. Sel. Top. Quantum Electron.* **2022**, *28*, 8200317.
[3] P. Prabhathan, K. V. Sreekanth, J. Teng, J. H. Ko, Y. J. Yoo, H.-H. Jeong, Y. Lee, S. Zhang, T. Cao, C.-C. Popescu, B. M., T. Gu, Z. Fang, R. Chen, H. Tong, Y. Wang, Q. He, Y. Lu, Z. Liu, H. Y. Mandal, Y. Cui, A. S. Ansari, V. Bhingardive, M. Kang, C. K. Lai, M. Merklein, M. J. Müller, Y. M. Song, Z. Tian, J. Hu, M. Losurdo, *iScience* **2023**, *26*, 107946.
[4] C. Ríos, M. Stegmaier, P. Hosseini, D. Wang, T. Scherer, C. D. Wright, H. Bhaskaran, W. H. Pernice, *Nat. Photonics* **2015**, *9*, 725.
[5] W. H. Pernice, H. Bhaskaran, *Appl. Phys. Lett.* **2012**, *101*, 171101.
[6] S. R. Ovshinsky, *Phys. Rev. Lett.* **1968**, *21*, 1450.
[7] S. Raoux, *Annu. Rev. Mater. Res.* **2009**, *39*, 25.
[8] M. Wuttig, N. Yamada, *Nat. Mater.* **2007**, *6*, 824.
[9] N. Yamada, E. Ohno, K. Nishiuchi, N. Akahira, M. Takao, *J. Appl. Phys.* **1991**, *69*, 2849.
[10] S. Raoux, G. W. Burr, M. J. Breitwisch, C. T. Rettner, Y.-C. Chen, R. M. Shelby, M. Salinga, D. Krebs, S.-H. Chen, H.-L. Lung, *IBM J. Res. Dev.* **2008**, *52*, 465.
[11] B. J. Kooi, M. Wuttig, *Adv. Mater.* **2020**, *32*, e1908302.
[12] M. Wuttig, H. Bhaskaran, T. Taubner, *Nat. Photonics* **2017**, *11*, 465.
[13] M. Delaney, I. Zeimpekis, D. Lawson, D. W. Hewak, O. L. Muskens, *Adv. Funct. Mater.* **2020**, *30*, 2002447.
[14] W. Dong, H. Liu, J. K. Behera, L. Lu, R. J. Ng, K. V. Sreekanth, X. Zhou, J. K. Yang, R. E. Simpson, *Adv. Funct. Mater.* **2019**, *29*, 1806181.
[15] W. Jia, R. Menon, B. Sensale-Rodriguez, *Opt. Mater. Express* **2021**, *11*, 3007.
[16] P. Moitra, Y. Wang, X. Liang, L. Lu, A. Poh, T. W. Mass, R. E. Simpson, A. I. Kuznetsov, R. Paniagua-Dominguez, *Adv. Mater.* **2023**, *35*, 2205367.
[17] X. Yang, L. Lu, Y. Li, Y. Wu, Z. Li, J. Chen, L. Zhou, *Adv. Funct. Mater.* **2023**, *33*, 2304601.
[18] M. J. Müller, A. Yadav, C. Persch, S. Wahl, F. Hoff, M. Wuttig, *Adv. Electron. Mater.* **2022**, *8*, 2100974.
[19] L. Guarneri, S. Jakobs, A. von Hoegen, S. Maier, M. Xu, M. Zhu, S. Wahl, C. Teichrib, Y. Zhou, O. Cojocaru-Mirédin, *Adv. Mater.* **2021**, *33*, 2102356.
[20] J.-Y. Raty, C. Bichara, C.-F. Schön, C. Gatti, M. Wuttig, *Proc. Natl. Acad. Sci. USA* **2024**, *121*, e2316498121.
[21] O. Cojocaru-Mirédin, Y. Yu, J. Köttgen, T. Ghosh, C. F. Schön, S. Han, C. Zhou, M. Zhu, M. Wuttig, *Adv. Mater.* **2024**, *36*, 2403046.
[22] B. Huang, J. Robertson, *Phys. Rev. B: Condens. Matter Mater. Phys.* **2010**, *81*, 081204.
[23] K. Shportko, S. Kremers, M. Woda, D. Lencer, J. Robertson, M. Wuttig, *Nat. Mater.* **2008**, *7*, 653.
[24] M. Zhu, O. Cojocaru-Mirédin, A. M. Mio, J. Keutgen, M. Küpers, Y. Yu, J. Y. Cho, R. Dronskowski, M. Wuttig, *Adv. Mater.* **2018**. *30*, 1706735.
[25] M. Wuttig, C. F. Schön, J. Lötfering, P. Golub, C. Gatti, J. Y. Raty, *Adv. Mater.* **2023**, *35*, 2208485.
[26] R. Boughalmi, A. Boukhachem, M. Kahlaoui, H. Maghraoui, M. Amlouk, *Mater. Sci. Semicond. Process.* **2014**, *26*, 593.
[27] Y. Gutiérrez, A. P. Ovvyan, G. Santos, D. Juan, S. A. Rosales, J. Junquera, P. García-Fernández, S. Dicorato, M. M. Giangregorio, E. Dilonardo, F. Palumbo, M. Modreanu, J. Resl, O. Ishchenko, G. Garry, T. Jonuzi, M. Georghe, C. Cobianu, K. Hingerl, C. Cobet, F. Moreno, W. H. P. Pernice, M. Losurdo, *iScience* **2022**, *25*, 104377.
[28] K. Liu, Z. Lin, B. Han, M. Hong, T. Cao, *Opto-Electronic Adv.* **2024**, *7*, 230033.
[29] L. Lu, S. F. Reniers, Y. Wang, Y. Jiao, R. E. Simpson, *J. Opt.* **2022**, *24*, 094001.
[30] M. J. Müller, C. Morell, P. Kerres, M. Raghuwanshi, R. Pfeiffer, S. Meyer, C. Stenz, J. Wang, D. N. Chigrin, P. Lucas, *Adv. Funct. Mater.* **2024**, *34*, 2403476.
[31] M. Xu, X. Mai, J. Lin, W. Zhang, Y. Li, Y. He, H. Tong, X. Hou, P. Zhou, X. Miao, *Adv. Funct. Mater.* **2020**, *30*, 2003419.
[32] H. L. Smith, C. W. Li, A. Hoff, G. R. Garrett, D. S. Kim, F. C. Yang, M. S. Lucas, T. Swan-Wood, J. Y. Lin, M. B. Stone, *Nat. Phys.* **2017**. *13*, 900.
[33] J. Pries, S. Wei, F. Hoff, P. Lucas, M. Wuttig, *Scr. Mater.* **2020**, *178*, 223.
[34] S. Wei, P. Lucas, C. Austen Angell, *J. Appl. Phys.* **2015**, *118*, 034903.
[35] H. E. Kissinger, *J. Res. Natl. Bur. Stand.* **1956**, *57*, 217.
[36] H. E. Kissinger, *Anal. Chem.* **1957**, *29*, 1702.
[37] J. Pries, H. Weber, J. Benke-Jacob, I. Kaban, S. Wei, M. Wuttig, P. Lucas, *Adv. Funct. Mater.* **2022**, *32*, 2202714.
[38] J. Pries, S. Wei, M. Wuttig, P. Lucas, *Adv. Mater.* **2019**, *31*, 1900784.

[39] J. Pries, Y. Yu, P. Kerres, M. Häser, S. Steinberg, F. Gladisch, S. Wei, P. Lucas, M. Wuttig, *Phys. Status Solidi RRL* **2020**. *15*, 2000478.
[40] J. Pries, J. C. Sehringer, S. Wei, P. Lucas, M. Wuttig, *Mater. Sci. Semicond. Process.* **2021**, *134*, 105990.
[41] G. W. Scherer, *Relaxation in Glass and Composites*, John Wiley & Sons, Inc., New York **1986**.
[42] Y. Yue, *J. Non-Cryst. Solids: X* **2022**, *14*, 100099.
[43] G. W. Scherer, *J. Non-Cryst. Solids* **1990**, *123*, 75.
[44] P. Lucas, S. Wei, C. A. Angell, *Int. J. Appl. Glass Sci.* **2020**, *11*, 236.
[45] J. Pries, C. Stenz, L. Schäfer, A. Gutsche, S. Wei, P. Lucas, M. Wuttig, *Adv. Funct. Mater.* **2022**, *32*, 2207194.
[46] G. W. Scherer, *J. Am. Ceram. Soc.* **1986**, *69*, 374.
[47] C. A. Angell, *Chem. Rev.* **2002**, *102*, 2627.
[48] C. T. Moynihan, *Rev. Mineral.* **1995**, *32*, 1.
[49] C. Moynihan, S.-K. Lee, M. Tatsumisago, T. Minami, *Thermochim. Acta* **1996**, *280*, 153.
[50] L. M. Wang, V. Velikov, C. A. Angell, *J. Chem. Phys.* **2002**, *117*, 10184.
[51] G. S. Fulcher, *J. Am. Ceram. Soc.* **1925**, *8*, 339.
[52] G. Tammann, W. Hesse, Z. Anorg, *Allg. Chem.* **1926**, *156*, 245.
[53] H. Vogel, *Phys. Z.* **1921**, *22*, 645.
[54] C. A. Angell, *Science* **1995**, *267*, 1924.
[55] M. Kassem, C. J. Benmore, A. Tverjanovich, T. Usuki, M. Khomenko, D. Fontanari, A. Sokolov, K. Ohara, M. Bokova, S. Kohara, E. Bychkov, *J. Mater. Chem. C* **2023**, *11*, 4654.
[56] C. K. Kelley, Thermal Analysis Study of Antimony Sulfides, Technical report, Wright Research and Development Center Wright-Patterson Air Force Base, Ohio **1989**.
[57] J. Bucaro, H. Dardy, *J. Non-Cryst. Solids* **1977**, *24*, 121.
[58] R. Böhmer, K. L. Ngai, C. A. Angell, D. J. Plazek, *J. Chem. Phys.* **1993**, *99*, 4201.
[59] C. Persch, M. J. Müller, A. Yadav, J. Pries, N. Honné, P. Kerres, S. Wei, H. Tanaka, P. Fantini, E. Varesi, *Nat. Commun.* **2021**, *12*, 4978.
[60] M. Salinga, E. Carria, A. Kaldenbach, M. Bornhofft, J. Benke, J. Mayer, M. Wuttig, *Nat. Commun.* **2013**, *4*, 2371.
[61] A. Sebastian, M. L. Gallo, D. Krebs, *Nat. Commun.* **2014**, *5*, 4314.
[62] P. Lucas, J. Pries, S. Wei, M. Wuttig, *J. Non-Crystalline Solids: X* **2022**, *14*, 100084.
[63] P. Lucas, W. Takeda, J. Pries, J. Benke-Jacob, M. Wuttig, *J. Chem. Phys.* **2023**, *158*, 054502.
[64] D. W. Henderson, *J. Non-Cryst. Solids* **1979**, *30*, 301.
[65] R. L. Blaine, H. E. Kissinger, *Thermochim. Acta* **2012**, *540*, 1.
[66] J. Orava, A. L. Greer, *Thermochim. Acta* **2015**, *603*, 63.
[67] P. G. Debenedetti, F. H. Stillinger, *Nature* **2001**, *410*, 259.
[68] J. Pries, J. Mayer, M. Wuttig, *Interplay of Glass Dynamics and Crystallization Kinetics in Amorphous Phase Change Materials*, Fachgruppe Physik, Springer, Berlin **2022**.
[69] H. J. Borchardt, F. Daniels, *J. Am. Chem. Soc.* **1957**, *79*, 41.
[70] W. A. Johnson, *Trans. Am. Inst. Min. Metall. Eng.* **1939**, *135*, 416.
[71] M. Avrami, *J. Chem. Phys.* **1939**, *7*, 1103.
[72] M. Avrami, *J. Chem. Phys.* **1940**, *8*, 212.
[73] M. Avrami, *J. Chem. Phys.* **1941**, *9*, 177.
[74] A. Kolomogorov, *Izv. Kazan. Fil. Akad. Nauk SSSR, Ser. Fiz.-Mat. Tekh. Nauk* **1937**, *3*, 355.
[75] M. Fanfoni, M. Tomellini, *Il Nuovo Cimento D* **1998**, *20*, 1171.
[76] J. Christian, *The Theory of Transformations in Metals and Alloys*, Newnes, New South Wales **2002**.
[77] A. Taute, S. Al-Jibouri, C. Laprais, S. Monfray, J. Lumeau, A. Moreau, X. Letartre, N. Baboux, G. Saint-Girons, L. Berguiga, S. Cueff, *Opt. Mater. Express* **2023**, *13*, 3113.
[78] T. Y. Teo, N. Li, L. Y. Tobing, A. S. K. Tong, D. K. T. Ng, Z. Ren, C. Lee, L. Y. T. Lee, R. E. Simpson, *ACS Photonics* **2023**, *10*, 3203.
[79] M. Wuttig, V. L. Deringer, X. Gonze, C. Bichara, J.-Y. Raty, *Adv. Mater.* **2018**, *30*, 1803777.
[80] P. Kerres, Y. Zhou, H. Vaishnav, M. Raghuwanshi, J. Wang, M. Häser, M. Pohlmann, Y. Cheng, C. F. Schön, T. Jansen, *Small* **2022**, *18*, 2201753.
[81] J.-Y. Raty, C. Bichara, C.-F. Schön, C. Gatti, M. Wuttig, *Proc. Natl. Acad. Sci. U. S. A.* **2024**, *121*, e2405294121.
[82] W. H. Zachariasen, *J. Am. Chem. Soc.* **1932**, *54*, 3841.